VELOCITY ANISOTROPY OF TWO DEEP CRYSTALLINE SAMPLES

by

Jim Mendelson and M.N. Toksöz

Earth Resources Laboratory
Department of Earth, Atmospheric, and Planetary Sciences
Massachusetts Institute of Technology
Cambridge, MA 02139

ABSTRACT

Using ultrasonic velocity measurements taken over a multiplicity of directions we show that samples exhibit weak to moderate anisotropy of seismic velocities. We further define the anisotropic geometry with high resolution scanning electron microscopy. Our data indicate that one sample, a granite, is transversely anisotropic, and that the presence of fine to moderately fine microcracks is the most important factor effecting the velocities. We model the angular velocity dependence using 5 elastic constants and show that all 9 observed velocities fit these predictions to within 0.1 km/s. We are unable to obtain similar fits to a second sample, a mica-schist, in the same fashion. SEM observations indicate this rock displays orthorhombic symmetry. We made additional velocity measurements in order to calculate 9 elastic constants, and found that the predicted angular velocity dependence agreed much better with our velocity observations.

INTRODUCTION

It has been known for a long time that velocity anisotropy is present in the majority of the solid earth (e.g., Crampin, 1977). Anisotropy is often related to local stresses, due for instance to mineral or grain alignments or preferential flow directions. Because of this, the study of anisotropy yields important information in seismology and structural geology. In this paper we examine the nature and causes of anisotropy observed in two deep borehole samples from the Larderello geothermal field, Italy. Using a multiplicity of ultrasonic velocity measurements and SEM images, we propose anisotropic models for each sample. Based on our data, one sample (a granite) possesses approximately hexagonal symmetry, whilst a second (mica-schist) is approximately orthorhombic.

I have found studies of this type relatively limited in the literature. One relevant study is Thill et al. (1969), which observed correlations between rock fabric and P-

velocities measured on spherical samples. Olivine (orthorhombic) is particularly well studied, and it's nine elastic constants were first reported by Verma (1960). Those results are widely used in studying the ocean crust and upper mantle. Most of the theory of anisotropic wave propagation was worked out by the early twentieth century by Kelvin, Christoffel, Stoneley, Reuss, Rudski, and others. Good reviews of the theory include Musgrave (1970) and Auld (1973). The case of weak anisotropy is discussed in Thomsen (1986). Many recent papers have investigated the occurrence of transverse isotropy (hexagonal symmetry) in velocity data, including Lo et al. (1986) and White et al. (1983), but none of these deal with more complicated symmetry systems.

Our velocity data and SEM images both suggest the mica-schist sample shows orthorhombic symmetry. We will compare transversely isotropic (TI) and orthorhombic models for both samples in the sections below. Before doing this, we briefly review the theory and methods of data acquisition.

BRIEF REVIEW OF ANISOTROPIC WAVE PROPAGATION

The simplest case arises when the coordinate planes of stress σ are aligned with the symmetry planes of the medium. The force balance equation is then

$$\sigma_{ij,j} + \rho X_j = \rho \ddot{u}_i \tag{1}$$

where ρ is density, u is displacement, and X_j is a body force. The comma [","] stands for differentiation with respect to subsequent indices. For a uniform, purely elastic solid, stress is related to strain by the constitutive relation,

$$\sigma_{ij} = c_{ijrs} u_{r,s} \; . \tag{2}$$

c_{ijrs} is the fourth rank elastic stiffness tensor. Combining (1) and (2) yields the equations of motion. In the absence of body forces,

$$c_{ijrs} u_{r,sj} = \rho \ddot{u}_i \; . \tag{3}$$

We further confine our study to plane wave solutions of the form

$$u_j = a_j \exp\left[i\left(k_r x_r - \omega t\right)\right], \qquad j, r = 1, 2, 3 \; . \tag{4}$$

Substituting our trial solution (4) into the equations of motion (3) yields the Christoffel equation:

$$\left[k^2 \Gamma ij - \rho\omega^2 \delta_{ij}\right] v_j = 0 \; . \tag{5}$$

Γ_{ij} is called the Christoffel matrix; it depends on the elastic constants and the direction cosines (l_{ij}) of the propagation vector. δ_{ij} is the kroenecker delta. If (5) is to have real roots, we require that the determinant

$$\left|\Gamma ij(l_x, l_y, l_z) - \rho c^2 \delta_{ij}\right| = 0 \; . \tag{6}$$

Notice we have replaced k^2/ω^2 by c^2. The determinant is a cubic in ρc^2 and the three real roots correspond to the phase velocities of a P- and two S-waves in a particular direction.

Symmetry and the Stiffness Tensor

c_{ijrs} is the fourth rank elastic stiffness tensor, which has 81 components. Because of the definition of infinitessimal strains, and the requirement that there be no net rotation in the body, we find $c_{ijrs} = c_{jirs}$ and $c_{ijrs} = c_{ijsr}$. This reduces to 36 the number of independent elastic constants. The existence of a unique strain energy function requires that $c_{ijrs} = c_{rsij}$, further reducing the number of independent constants to 21. That is the number of elastic constants necessary to describe propagation in most monoclinic crystals. In the remainder of this paper we use reduced suffix notation to write the elements of the elastic tensor. The reduced suffixes take the form

$$\begin{array}{llll} 11 \rightarrow 1 & & 23,32 \rightarrow 4 \\ 22 \rightarrow 2 & & 13,31 \rightarrow 5 \\ 33 \rightarrow 3 & & 12,21 \rightarrow 6 \end{array}$$

and the abbreviated stress-strain relation is $\sigma_p = c_{pq} e_q$.

Hexagonally symmetric media have five non-zero elastic constants,

$$\begin{pmatrix} c_{11} & c_{12} & c_{13} & 0 & 0 & 0 \\ c_{12} & c_{11} & c_{13} & 0 & 0 & 0 \\ c_{13} & c_{13} & c_{33} & 0 & 0 & 0 \\ 0 & 0 & 0 & c_{44} & 0 & 0 \\ 0 & 0 & 0 & 0 & c_{44} & 0 \\ 0 & 0 & 0 & 0 & 0 & \frac{1}{2}(c_{11} - c_{12}) \end{pmatrix} . \tag{7}$$

The additional symmetry is the result of one mirror plane and one rotational axis.

Orthorhombic media have nine non-zero elastic constants,

$$\begin{pmatrix} c_{11} & c_{12} & c_{13} & 0 & 0 & 0 \\ c_{12} & c_{22} & c_{23} & 0 & 0 & 0 \\ c_{13} & c_{23} & c_{33} & 0 & 0 & 0 \\ 0 & 0 & 0 & c_{44} & 0 & 0 \\ 0 & 0 & 0 & 0 & c_{55} & 0 \\ 0 & 0 & 0 & 0 & 0 & c_{66} \end{pmatrix} . \tag{8}$$

Additional symmetry with respect to monoclinic crystals is the result of three perpendicular mirror planes.

DESCRIPTION OF SAMPLES AND DATA

An igneous rock (granite) and a metamorphic rock (mica-schist) were cored at depths of 3.5 and 2.9 km respectively, from boreholes used to extract superheated steam reserves for power generation near Larderello, Italy. Larderello (see Figure 1) lies southeast of Pisa, between the Apennines and the Tyrrhenian Sea, near the center of a high heat flow anomaly (Batini et al., 1983). The area is the oldest and one of the largest developments of geothermal electricity generation, and because of this it is an important area for development.

Both samples, the granite and the mica-schist, were re-cored in 3 directions: $0^o, 45^o$, and 90^o to foliation. These 1" by 1" cores were cut and ground parallel for velocity measurements. End pieces were polished to 0.1 micron and carbon-coated for electron microscope analysis.

Sample descriptions by SEM

Figures 2 and 3 show high resolution (100 lines/inch) electron backscatter images of each sample parallel to and perpendicular to foliation. Magnifications are indicated by the scale bars in each photo. The grey levels in the images are proportional to the average atomic number of the grains (Pye and Krinsley, 1984). Mineral identification is further enhanced by obtaining a characteristic X-ray spectrum of the constituent elements illuminated by the probe's beam. Combining these two techniques it is possible to establish approximate mineral percentage on a digitized micrograph. The dominant minerals in the granite are quartz, plagioclase, orthoclase, and mica. The mica-schist is mostly mica with quartz and plagioclase. Photos of the foliation plane in the mica-schist show a composition almost entirely of mica and quartz. Only the photos perpendicular to the mica-schist foliation planes reveal that a substantial amount of plagioclase is also present. Table 1 summarizes the results of SEM mineral identification.

Table 1: Microprobe estimates of major mineral fractions (%).

pore	quartz	plagioclaise	orthoclaise	mica	
2.38	40.4	26.6	19.6	6.36	Granite, n=9
4.21	54.5			35.2	Mica-schist, n=7

It should be pointed out that the electron beam penetrates the sample to a depth of only a few microns, so the technique is effectively 2-D. Potentially large errors could

result in extrapolating to 3 dimensions. In creating Table 1 we attempt to minimize this error by averaging the results of many 2-D areas (Wissler, 1987).

In the granite sample, porosity by wet and dry weighing at room conditions was 1.13% which is lower than the digital image estimate of 2.38%. A typical image (Figure 2) reveals the majority of the pores are flat cracks, but rounder intergranular pores are also common. Microcracks are not generally parallel. Some of the cracks are filled with micas, indicating fluid circulation took place. When a crack does not display any mineralization, it can be argued the crack was created while retrieving or preparing the sample. A basic argument is that stresses due to cooling or unloading the sample during retrieval cause dilitational cracking. We examined a typical microcrack in a feldspar grain (Figure 4) and concluded the crack faces show signs of weathering and probably were not freshly created. The high magnification image in Figure 4 (2000x), in secondary electron mode, has improved depth of field but no grey level to mean atomic number relation. There are very few aligned features (either grains or cracks) observed in the SEM photos of the granite. One exception is the presence of moderately and highly aligned perthite (Figure 4). Perthite is a solid solution of orthoclase-plagioclase formed by exsolution on cooling. Albite laminae generally form parallel to the cleavage plane in the orthoclase background, and are not directly controlled by stress directions. More rarely perthite textures are controlled by metasomatism, and in this case flow directions may be parallel to a principal stress direction.

Although it contains many of the same minerals as the granite, the mica-schist has a very different texture. The mica-schist is composed mostly of quartz, plagioclase, and mica (see Table 1). The mica group is dominantly biotite and muscovite, with somewhat less chlorite. Figure 3 shows immediately that there are large numbers of aligned features both in and at right angles to the schistosity plane. This is the first indication that the rock may possess orthorhombic symmetry. In the upper photo in Figure 3 we see the largest faces of the micas. Under conditions of nonhydrostatic stress, these develop perpendicular to the least principal stress. There is also moderate alignment of the long axes of quartz grains in this plane. In the lower photo, perpendicular to schistosity, we see more micas end-on. There is also a considerable fraction of sodium feldspar not seen in the bedding plane. The tab-shaped pores which were common in the granite are replaced by more sub-equant pores and some low aspect ratio (width/length $\sim 10^{-1}$) cracks.

Laboratory Ultrasonic Analysis

Velocity measurements were acquired at $0°, 45°$, and $90°$ to the drillhole axis. Records were not maintained of the azimuthal orientation of the drilled core with respect to north. One compressional and two shear (with mutually perpendicular polarization) measurements were made for each orientation of the sample. The entire set of mea-

surements was repeated while varying the confining pressure on the sample between 100 and 750 bars at 100 bar increments. Using distilled water as a saturant, pore pressure was maintained at 50 bars throughout the experiment. The measuring system, described in Lo et al. (1986) operates at 1 MHz and is accurate to better than 1% (see Appendix for error analysis). Measured velocities as a function of pressure and orientation are given in the Appendix and also plotted in Figures 5 and 6. The geometry of the velocity observations with respect to the three cores is shown below.

P- and S-velocities as a function of pressure are typical of crystalline rocks: velocities rise fastest at low pressures and then behave asymptotically. Rapid increase in P-velocity at low pressures is primarily controlled by the closing of fine cracks. Shear velocities are less affected. At about 0.5 kb, most low aspect ratio cracks close in Troy Granite (Cheng, 1978). Dependences of velocity on pressure and saturation have been treated fully in Toksöz et al. (1976).

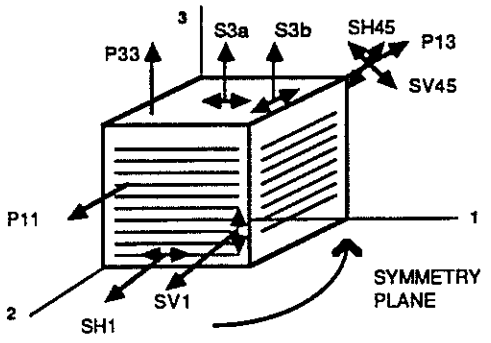

Both the granite and the mica-schist have P-velocity maxima in the P11 direction and minima in the P33 direction. SH1 is the fastest shear wave because both propagation and particle motion directions are in the foliation plane. From these data we compute the observed P- and S-velocity anisotropies in Table 2, which yield two important results.

Table 2: Observed anisotropy (%) of P- and S-waves.

	P-wave	S-wave
Granite, $P_e = 50$ bars	2.73	5.68
Granite, $P_e = 700$ bars	1.04	2.49
Schist, $P_e = 50$ bars	9.36	17.9
Schist, $P_e = 700$ bars	8.58	15.1

First, the mica-schist is considerably more anisotropic than the granite. This is expected, since biotite has measured velocities almost twice as fast in the foliation plane than at right angles to it (Simmons and Wang, 1971). Second, although weaker, anisotropy in the granite decreases by more than 60% as pressure increases over the range $P_{eff} = 50 \rightarrow 700$ bars. This is in sharp contrast to the mica-schist, where percent anisotropy remains nearly constant over the same range of pressures. This provides evidence that closing of microcracks that have preferred orientations is responsible for most of the observed anisotropy in the granite.

DISCUSSION OF RESULTS

This section is divided in two parts. In the first part we attempt to model each sample at low and high pressures as transversely isotropic. While the granite data fit this model reasonably well, the mica-schist data do not. In the second part, we describe additional velocity measurements we made in order to test an orthorhombic symmetry model. We also refer to SEM images and arguments based on structural geology to support the orthorhombic model. The data will show that the data fit this new model better than the TI model, but we still cannot recover the variability completely.

Transverse Isotropy

It is often convenient to assume a TI model of the earth, as it is a simple model for horizontal layering without lateral heterogeneity. Referring to the diagram on the preceding page, under this assumption the 1-2 plane is a symmetry plane, and any rotation about the 3–axis will not change the velocities. We can test these assumptions immediately by looking at the velocities S3a, S3b, and SV1. These should be equal because each vibrates or propagates in opposite (i.e., fast or slow) directions. Figures 5 and 6 show that the TI assumptions are much better justified in the granite than they are in the mica-schist.

If a medium is uniform, elastic, and TI, then the elastic constants can be calculated from only five velocities according to

$$C_{11} = \rho V_{11}^2, \tag{9}$$

$$C_{12} = C_{11} - \rho V_{sh1}^2, \tag{10}$$

$$C_{33} = \rho V_{p33}^2, \tag{11}$$

$$C_{44} = \rho V_{s3}^2, \tag{12}$$

$$C_{13} = -C_{44} + \sqrt{4\rho^2 V_{p45}^4 - 2\rho V_{p45}^2 (C_{11} + C_{33} + 2C_{44}) + (C_{11} + C_{44})(C_{33} + C_{44})} \tag{13}$$

Notice that there is no dependence in the calculated c_{ij} on SV1, or on the 45^o shear velocities SH45 and SV45. Thus these data can be used to investigate the adequacy of the TI model. The elastic constants calculated in this way are given below, subject to the uncertainties listed in the Appendix.

Table 3. TI elastic constants c_{ij} (Kbars)

	c_{11}	c_{33}	c_{44}	c_{12}	c_{13}
Granite, $P_e = 50$ bars	757.8	357.7	728.4	192.6	310.1
Granite, $P_e = 700$ bars	846.7	332.0	859.3	258.7	291.4
Schist, $P_e = 50$ bars	876.6	325.7	788.2	233.7	266.3
Schist, $P_e = 700$ bars	968.7	336.4	844.6	277.4	287.7

Using these constants it is straightforward to calculate phase velocities for any propagation vector. One can find eigenvalues of the Christoffel matrix (6) or solve the cubic (8). We show our results in Figures 7 and 8, where velocities are plotted as a function of angle above the horizontal plane. First considering the P-waves, we notice both samples show velocity minima at about 45°. This feature is most pronounced in the granite, again suggesting that open microcracks cause much of the observed anisotropy, especially at low pressures. The shear wave data (Figure 8) are less affected by the cracks. SH velocities increase from 0° to 90°, where both particle motion and propagation are aligned in the fast direction. SV minima occur at 0° and 90°, while the maxima at 45° occur when the largest components of propagation and particle motion are in the fast direction. We plot the observed 45° shear wave velocities as crosses to further test the validity of TI. While differences are small (compared to measurement error) for the granite, they are more than 0.3 km/s for the mica-schist. Thus we conclude that TI is not adequate to describe the mica-schist and a more complicated symmetry is needed.

Orthorhombic Isotropy

Orthorhombic symmetry can be used to describe many common geologic settings, including horizontal layering cut by vertical fractures. For this to occur we require only that the least compressive stress be horizontal (Nur, 1969). We also saw evidences in SEM images (Figure 3) and hand specimens of considerable vertical fracturing in the mica-schist. Therefore we attempt to model the velocity dependence of the mica-schist using orthorhombic symmetry. This requires nine elastic constants, which can be calculated from observable velocities using equations similar to (9-13) (Podio-Lucioni, 1969). Notice that we need to measure velocities perpendicular to all three symmetry planes, and at 45° to each pair of planes shown below.

We measured additional P- and S-velocities on cores in the 22, 23 and 12 directions. These data show that P-wave anisotropy in the horizontal plane is 3.7% at 50 bars and 1.2% at 700 bars. These additional data are also listed in the Appendix. With a total of 18 velocity measurements we calculate nine elastic constants according to

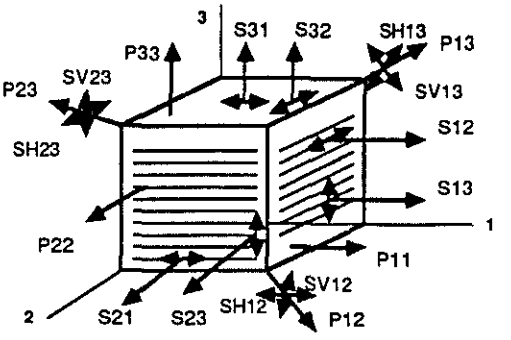

$$C_{11} = \rho V_{11}^2, \qquad C_{22} = \rho V_{22}^2, \qquad C_{33} = \rho V_{p33}^2, \tag{14}$$

$$C_{44} = \rho V_{s23}^2, \qquad C_{55} = \rho V_{s13}^2, \qquad C_{66} = \rho V_{s12}^2, \tag{15}$$

$$C_{13} = \left\{ \left[2\rho V_{p13|45^\circ}^2 - \frac{1}{2}(C_{11} + C_{33} + 2C_{55}) \right] - \left[\frac{C_{11} - C_{33}}{2} \right]^2 \right\}^{\frac{1}{2}} - C_{55} \tag{16}$$

$$C_{12} = \left\{ \left[2\rho V_{p12|45^\circ}^2 - \frac{1}{2}(C_{11} + C_{22} + 2C_{66}) \right] - \left[\frac{C_{11} - C_{22}}{2} \right]^2 \right\}^{\frac{1}{2}} - C_{66} \tag{17}$$

$$C_{23} = \left\{ \left[2\rho V_{p23|45^\circ}^2 - \frac{1}{2}(C_{22} + C_{33} + 2C_{44}) \right] - \left[\frac{C_{22} - C_{33}}{2} \right]^2 \right\}^{\frac{1}{2}} - C_{44} \tag{18}$$

Of course, if the medium is uniform, purely elastic, and orthorhombic we should find velocities S12 = S21, S23 = S32, and S13 = S31. Our data do not strictly follow these assumptions: the average difference between velocities S12 and S21 is 125 m/s; between S31 and S13, 255 m/s; and between S23 and S32, 16 m/s. We believe the most likely explanation for this discrepancy is sample inhomogeneity.

To further test the orthorhombic model we calculate the angular velocity dependence in each of the three principal planes. These results are shown in Figures 9 and 10. Additionally we plot all six 45° shear wave measurements in order to judge the fit to the model. Figure 9 shows that the 45° shear waves in the two vertical planes are fit quite well (less than 150 m/s error) but there is a larger error in the horizontal plane. For both low and high pressures (Figure 10) the model velocities are higher than the data. Some possible sources of this error are inhomogeneity, inaccuracy in cutting the 45° cores or aligning the transducers, or a previously unrecognized measurement error which pertains only to the 1-2 core.

CONCLUSIONS

We summarize the contributions of this work as follows. The granite sample behaves almost isotropically at pressures approximating in situ conditions (500–1000 bars). At

lower pressures, anisotropy in the granite is probably related to the preferential closing of microcracks in a direction normal to the maximum compressive stress. At higher pressures, anisotropy in the granite is weak, and is probably a smaller effect than measurement error. The mica-schist is intrinsically anisotropic at all pressures studied because of the high content of anisotropic minerals, particularly biotite. Hexagonal symmetry (i.e., transverse isotropy) permits reasonable modeling of the velocity data from both samples, but the evidence suggests orthorhombic symmetry is a better model for the mica-schist. Horizontal foliation is responsible for most of the observed anisotropy in the mica-schist, but vertical fractures contribute to anisotropy observed in the horizontal plane. This is supported by SEM images, and by the decrease in horizontal anisotropy with increasing pressure. Finally, mica-schist velocities predicted with an orthorhombic model agree better with laboratory ultrasonic data than do similar predictions from a TI model.

ACKNOWLEDGEMENTS

This work was supported in part by the Full Waveform Acoustic Logging Consortium at M.I.T., and by ENEL.

REFERENCES

Auld, B.A., *Acoustic Fields and Waves in Solids*, Wiley, New York, 1973.

Batini, F., G. Bertini, G. Gianelli, E. Pandeli, & M. Puxeddu, Deep structure of the Larderello field: contributions from recent geophysical and geological data, *Mem. Soc. Geo. It., 25* 219–235, 1983.

Cheng, C. H., *Seismic Velocities in Porous Rocks: Direct and Inverse Problems.,* Sc.D. thesis, Mass. Inst. of Tech., Cambridge, MA, 1978.

Christensen N., Compressional wave velocities in metamorphic rocks at pressures to 10 kilobars., *J. Geophys. Res., 70*, 6147–6164, 1965.

Crampin, S., A review of the effects of anisotropic layering on the propagation of seismic waves, *Geophys. J. Roy. Astr. Soc., 49*, 9–27, 1984.

Hadley, K., *Dilatancy: Further Studies in Crystalline Rocks,* Ph.D. thesis, Mass. Inst. of Tech., Cambridge, MA, 1975.

Hess, H., Seismic anisotropy of the uppermost mantle under oceans, *Nature, 203*, 629–631, 1964.

Lo, T., K. Coyner, and M. N. Toksöz, Experimental determination of elastic anisotropy of Berea sandstone, Chicòpee shale and Chelmsford granite, *Geophysics, 51*, 164–171, 1986.

Malvern, L.E., *Introduction to the Mechanics of a Continuous Medium*, Prentice-Hall, NJ, 1969.

Musgrave, M.J.P., *Crystal Acoustics*, Holden-Day, San Francisco, CA, 1970.

Nur, A., *Effects of Stress and Fluid Inclusions on Wave Propagation in Rock,* Ph.D. thesis, Mass. Inst. of Tech., Cambridge, MA, 1969.

Podio-Lucioni, A., *Experimental Determination of the Dynamic Elastic Properties of Anisotropic Rrocks, the Ultrasonic Pulse Method,* Ph.D. Thesis, Univ. Texas, Austin, TX, 1969.

Pye, K. and D.H. Krinsley, Petrographic examination of sedimentary rocks in the SEM using backscattered electron detectors, *J. Sed. Pet., 54*, 877–888, 1984.

Simmons G., and H. Wang, *Single Crystal Elastic Constants and Calculated Aggregate Properties*, M.I.T. Press, Cambridge, MA, 1971.

Thill, R.E., R.J. Willard and T.R. Bur, Correlation of longitudinal velocity variation

with rock fabric, *J. Geophys. Res., 74*, 4897, 1969.

Thomsen, L., Weak elastic anisotropy, *Geophysics, 51*, 1954–1966, 1986.

Toksöz, M.N., C.H. Cheng, and A. Timur, Velocities of seismic waves in porous rocks, *Geophysics, 41*, 621–645, 1976.

White, J.E., L. Martineau, and C. Monash Measured anisotropy in Pierre shale, *Geoph. Prospecting, 31* 709-725, 1983.

Wissler, T., *Sandstone Pore Structure: A Quantitative Analysis of Digital SEM Images*, Ph.D. thesis, Mass. Inst. of Tech, Cambridge, MA, 1987.

Appendix A. DATA AND ERROR ANALYSIS

Measurement	Nominal Value	Error	Percent Error
length	2.54 cm	0.01 cm	0.394
weight	35.00 g	0.01 g	0.029
arrival times			
T_p	5×10^{-6} s	1×10^{-8} s	0.200
T_s	8.333×10^{-6} s	1×10^{-8} s	0.120
Calculation			Percent Error
V_p			0.442
V_s			0.412
ρ			0.683
c_{11}, c_{22}, c_{33}			0.926
c_{44}, c_{55}, c_{66}			0.899
c_{13}			4.09
c_{12}			7.14
c_{23}			4.19

Granite Velocity Data

P_{eff}	P33	P11	S3a	S3b	P45
50	5.26	5.37	2.70	2.72	5.23
100	5.32	5.39	2.74	2.76	5.29
200	5.40	5.47	2.83	2.84	5.38
300	5.49	5.53	2.92	2.93	5.47
400	5.56	5.58	2.98	3.00	5.51
500	5.62	5.64	3.03	3.05	5.58
600	5.66	5.67	3.08	3.11	5.62
700	5.72	5.72	3.13	3.15	5.66

	SH1	SV1	SH45	SV45
50	2.76	2.77	2.72	2.76
100	2.82	2.78	2.77	2.80
200	2.90	2.86	2.86	2.91
300	2.97	2.93	2.93	2.97
400	3.03	2.99	2.99	3.04
500	3.09	3.05	3.05	3.08
600	3.13	3.10	3.10	3.14
700	3.17	3.14	3.13	3.17

Mica-Schist Velocity Data

Pressures are effective, i.e., confining minus pore pressure, in bars. Velocities are in km/sec.

P_{eff}	P33	S31	S32	P22	S21	S13
50	5.40	2.93	2.95	5.87	3.19	2.67
100	5.40	2.96	2.97	5.91	3.21	2.67
200	5.41	3.01	3.03	5.95	3.25	2.73
300	5.48	3.05	3.05	6.01	3.31	2.67
400	5.49	3.10	3.12	6.02	3.34	2.82
500	5.56	3.14	3.14	6.09	3.38	2.90
600	5.59	3.20	3.21	6.09	3.42	2.95
700	5.64	3.22	3.23	6.13	3.49	3.02

	S23	P13	SH45-13	SV45-13	P11	S12
50	2.96	5.39	2.97	2.97	5.91	3.37
100	2.98	5.45	3.00	2.98	5.91	3.38
200	3.04	5.49	3.04	3.05	5.98	3.41
300	3.07	5.58	3.10	3.09	5.99	3.43
400	3.12	5.60	3.14	3.15	6.03	3.46
500	3.14	5.67	3.18	3.16	6.06	3.48
600	3.18	5.70	3.21	3.21	6.11	3.52
700	3.19	5.75	3.23	3.23	6.12	3.54

	P12	P23	SH45-12	SV45-12	SH45-23	SV45-23
50	5.63	5.25	3.07	2.45	2.86	2.84
100	5.71	5.34	3.10	2.47	2.97	2.88
200	5.71	5.44	3.15	2.65	3.11	3.04
300	5.79	5.44	3.20	2.62	3.20	3.08
400	5.81	5.60	3.23	2.69	3.25	3.12
500	5.92	5.65	3.31	2.71	3.30	3.16
600	5.94	5.71	3.33	2.82	3.34	3.20
700	5.96	5.73	3.36	2.85	3.37	3.22

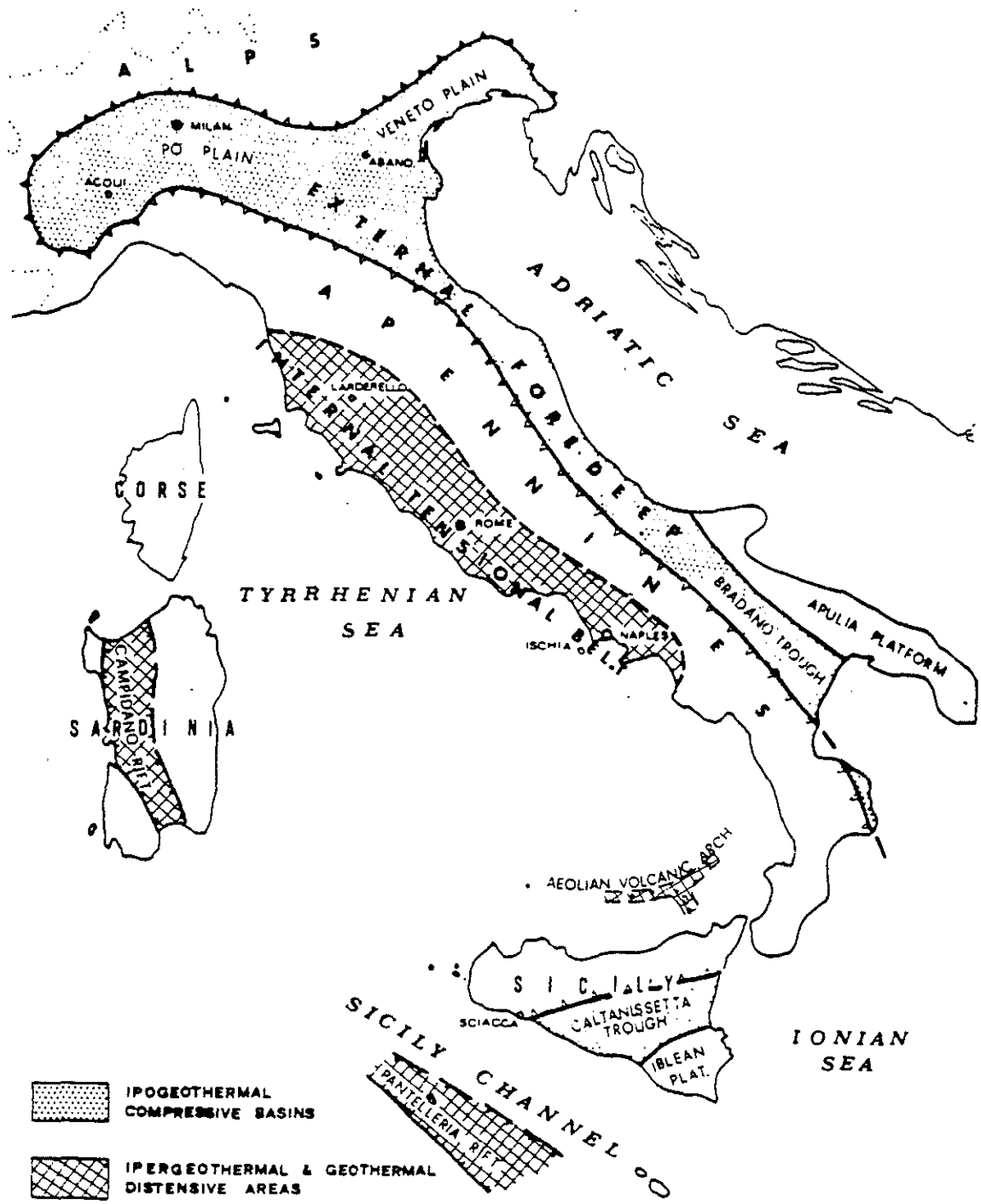

Figure 1: Regional map showing the location of the study area.

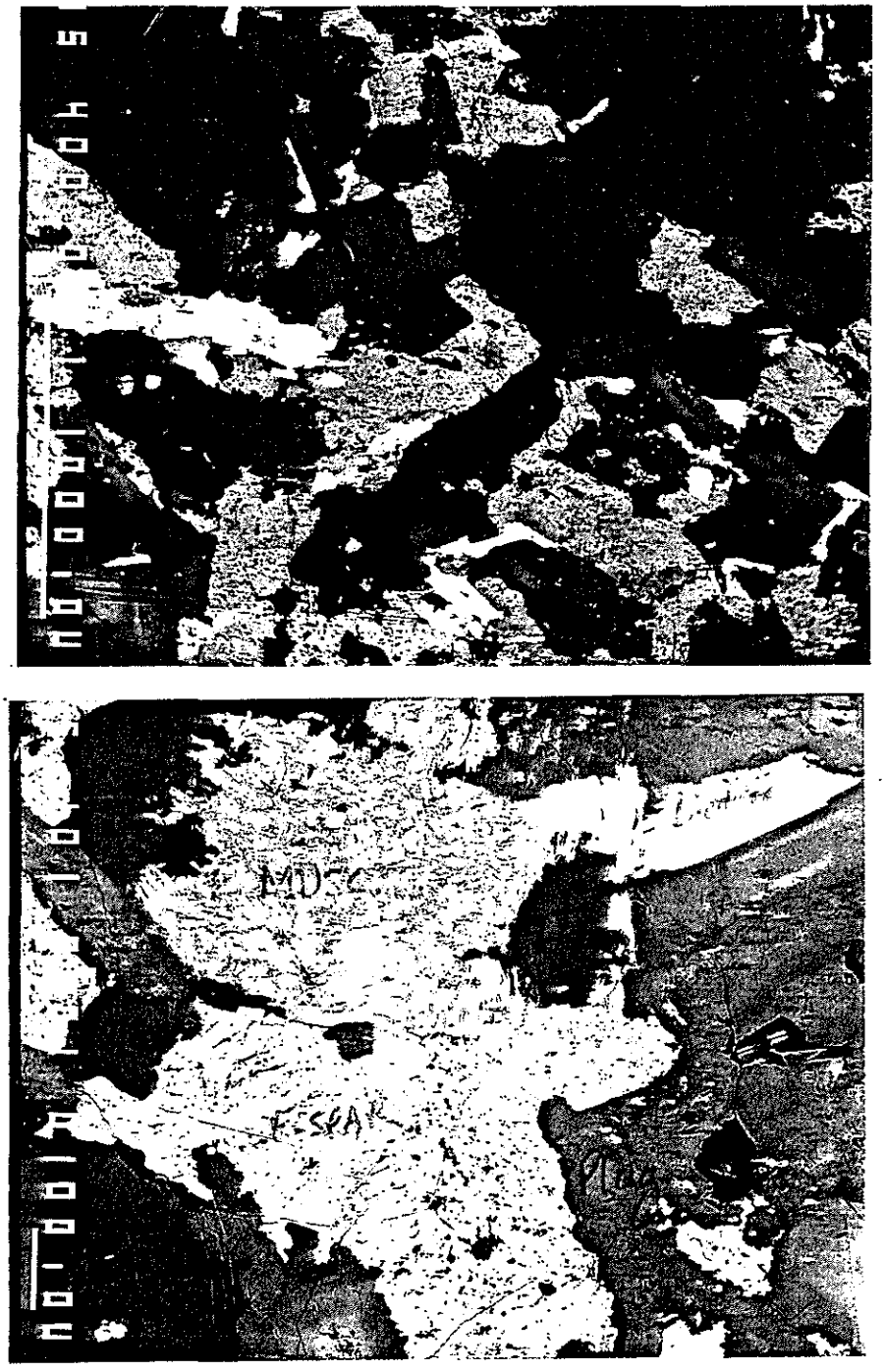

Figure 2: SEM images of the granite sample: top is vertical sample, bottom horizontal.

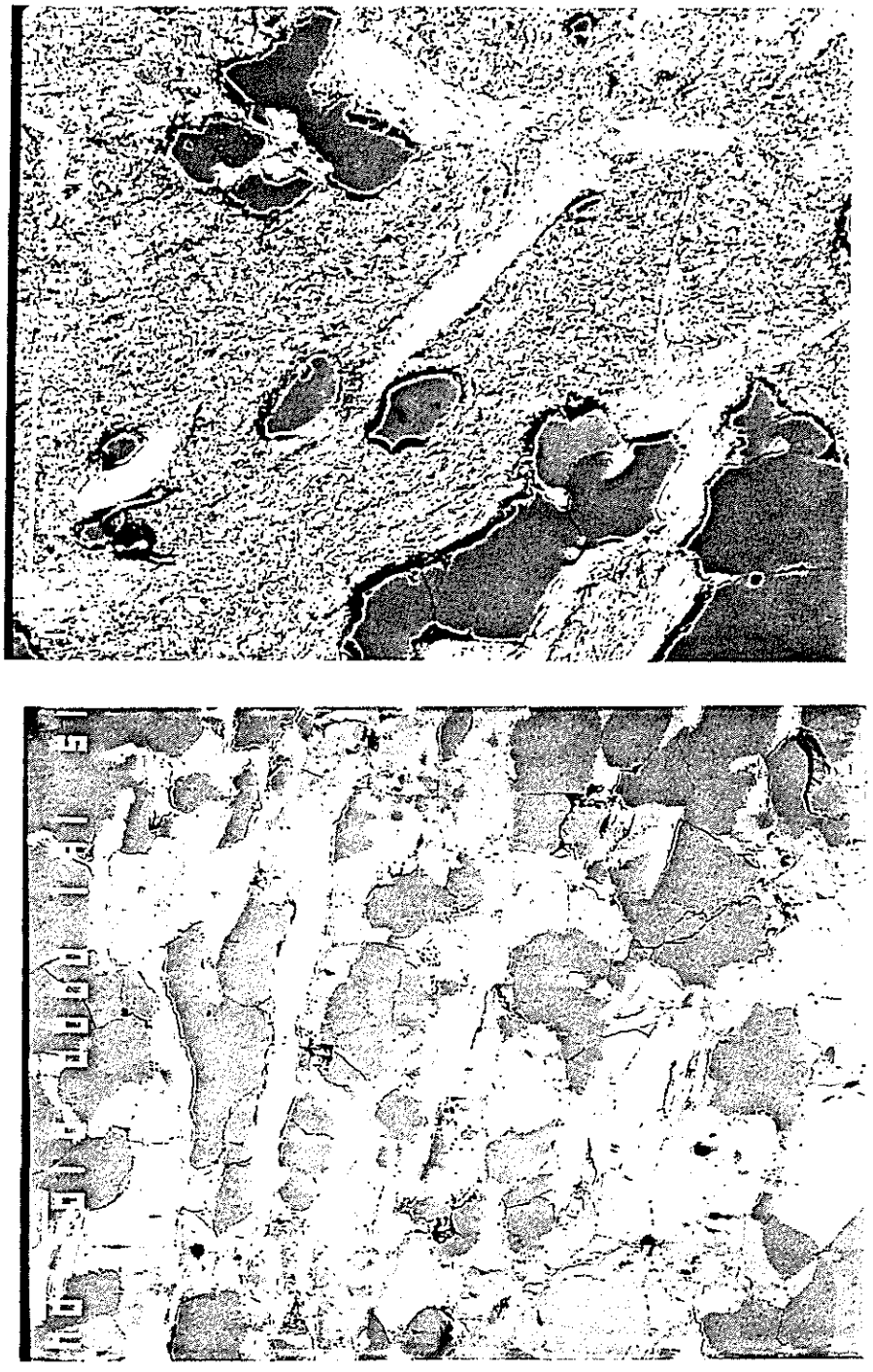

Figure 3: SEM images of the mica-schist sample: top is vertical sample, bottom horizontal.

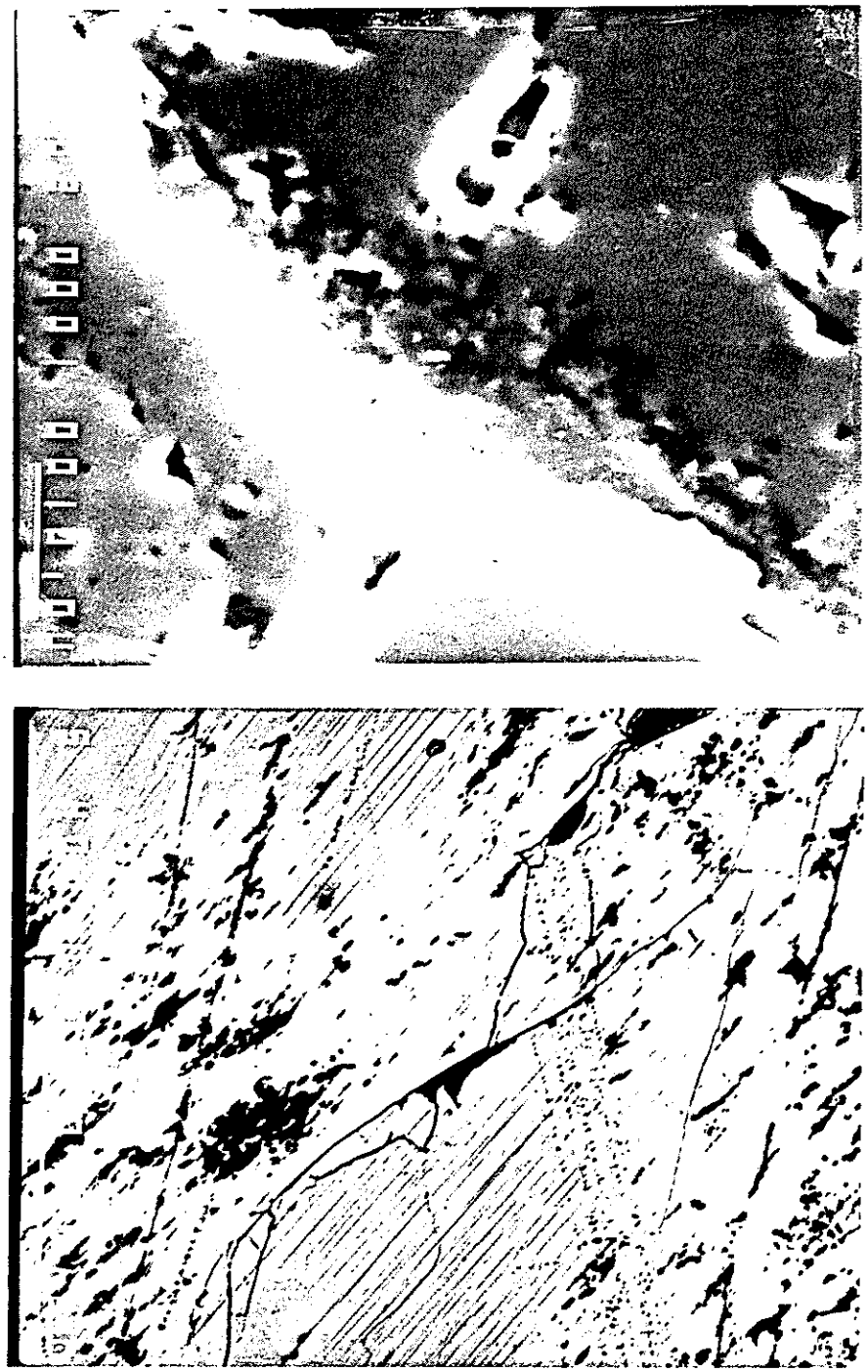

Figure 4: SEM images of the granite sample. Top: secondary electron image (2000X) of a microcrack. Bottom: backscatter image of highly aligned perthite.

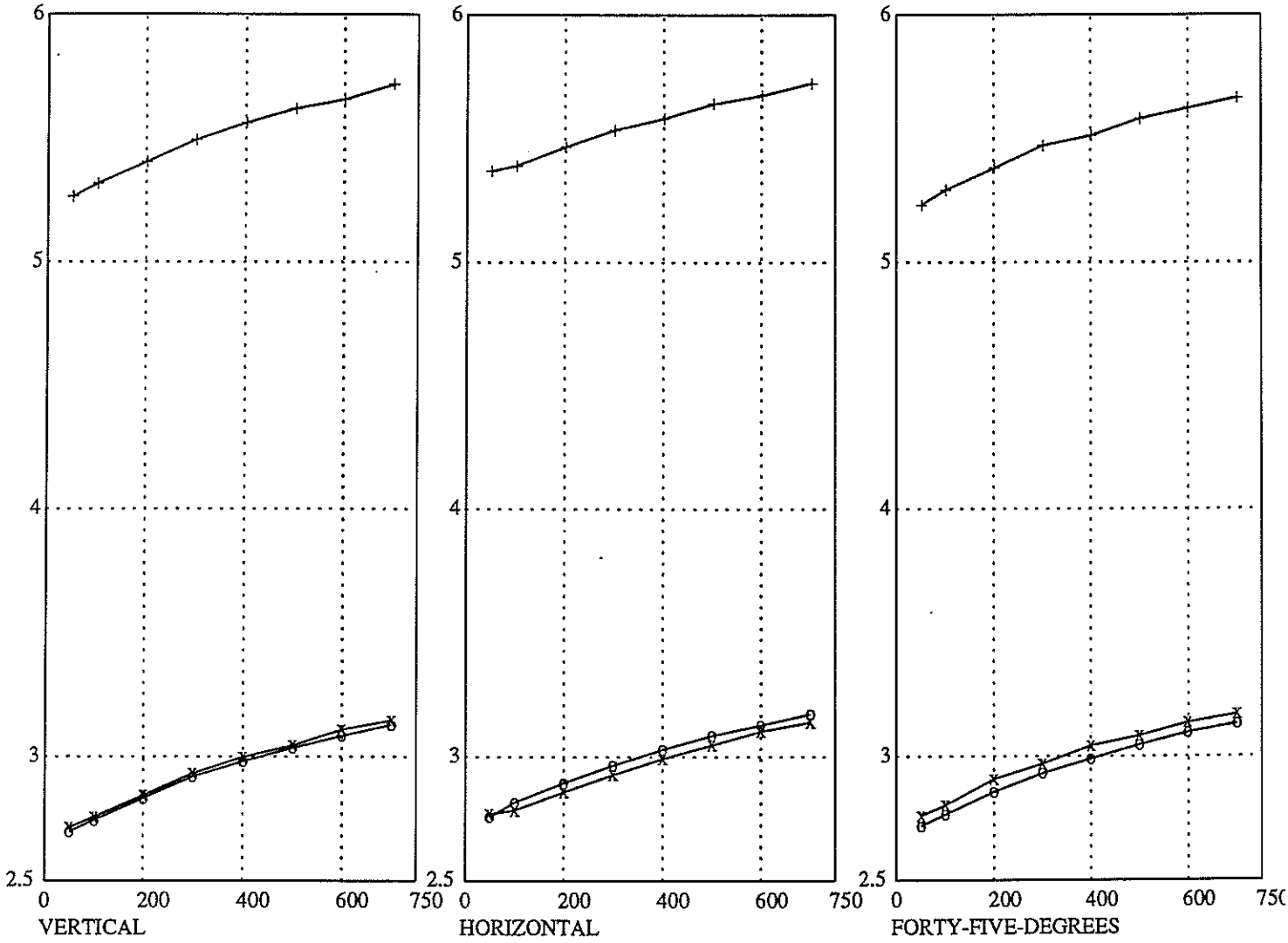

Figure 5: Velocities (km/s) as a function of pressure (bars), granite sample.

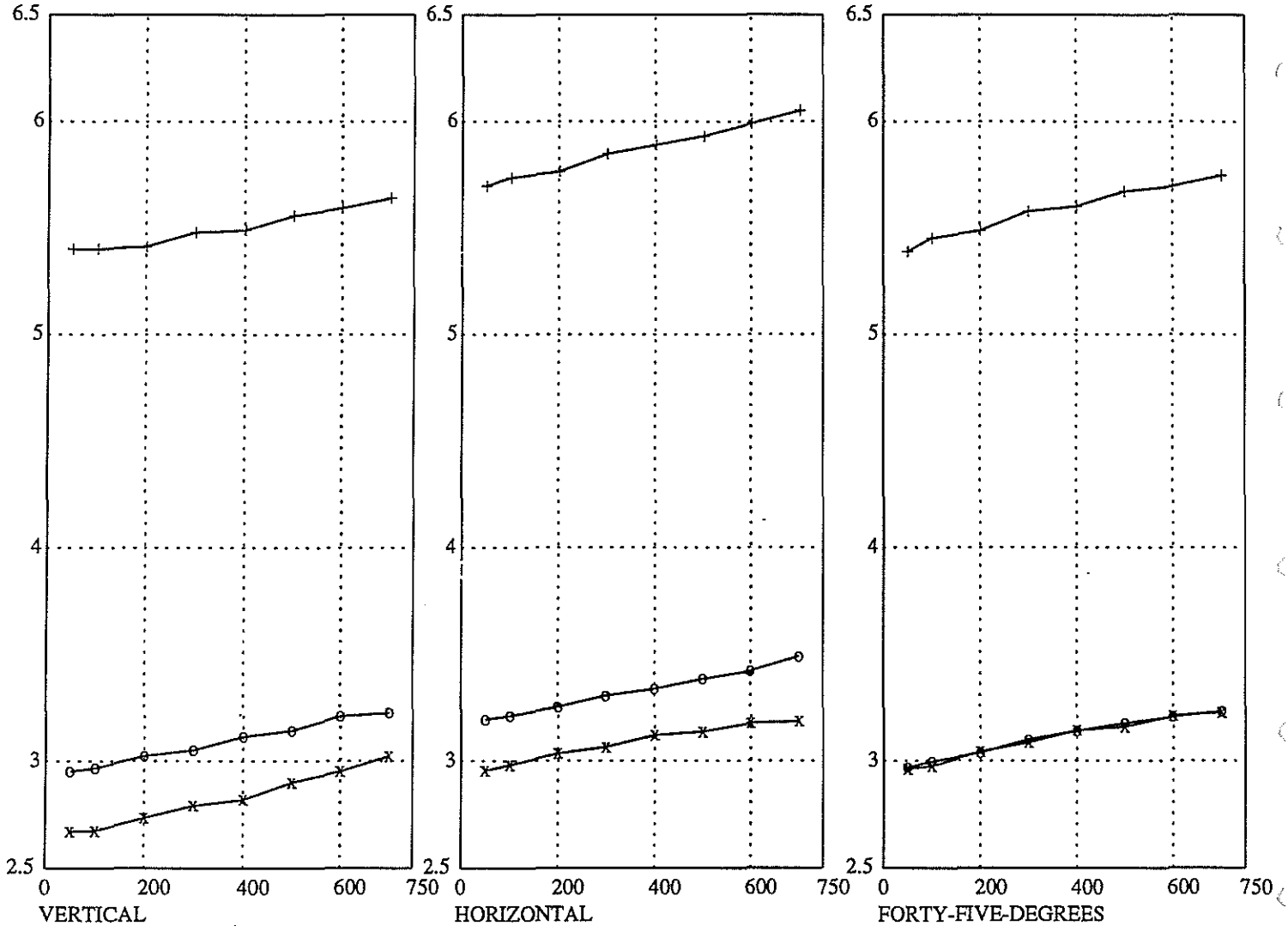

Figure 6: Velocities (km/s) as a function of pressure (bars), mica-schist sample.

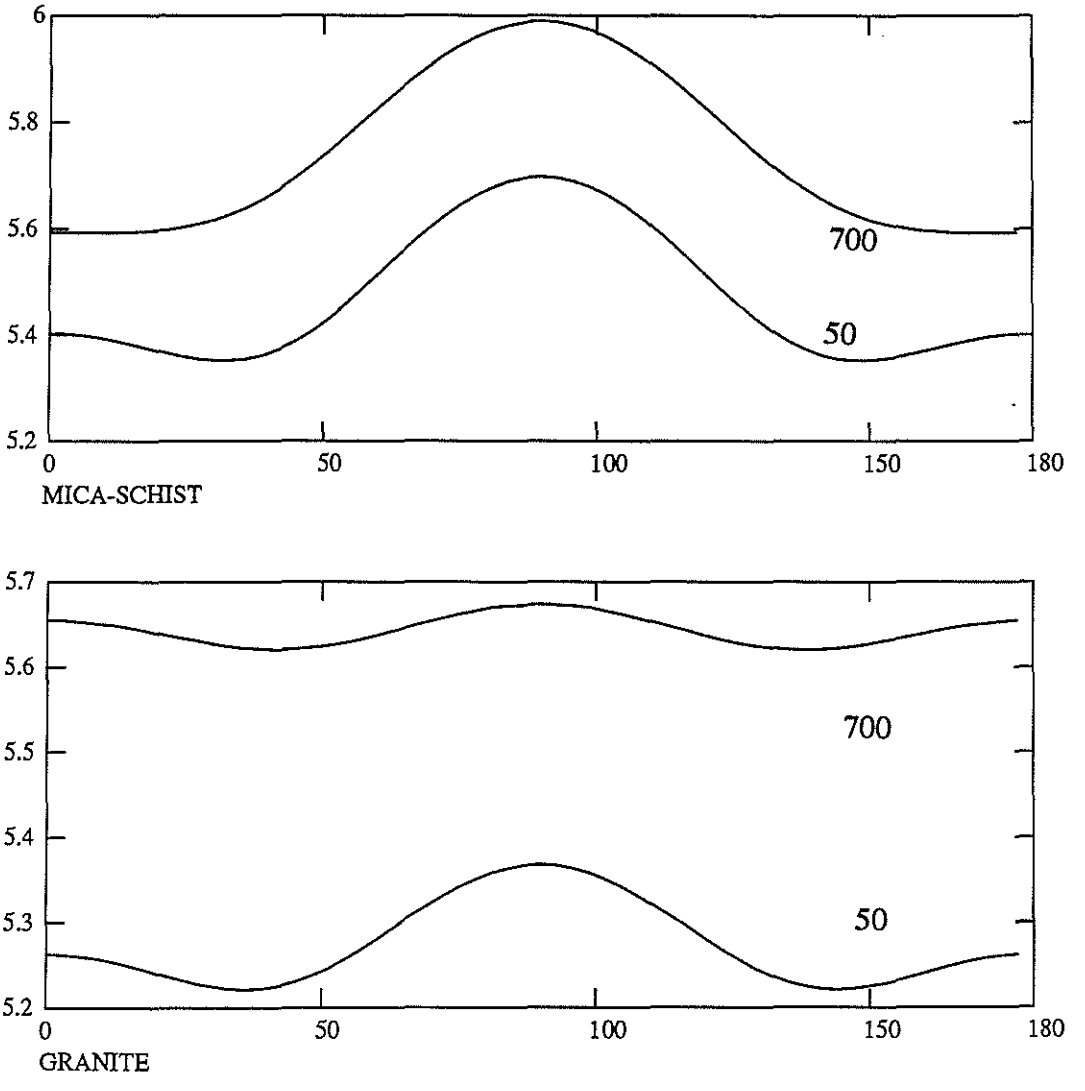

Figure 7: Transversely isotropic angular velocity dependence of P-waves, both samples, P_{eff}=50, 700 bars. Velocities in km/s. X-axis is angle above horizontal plane.

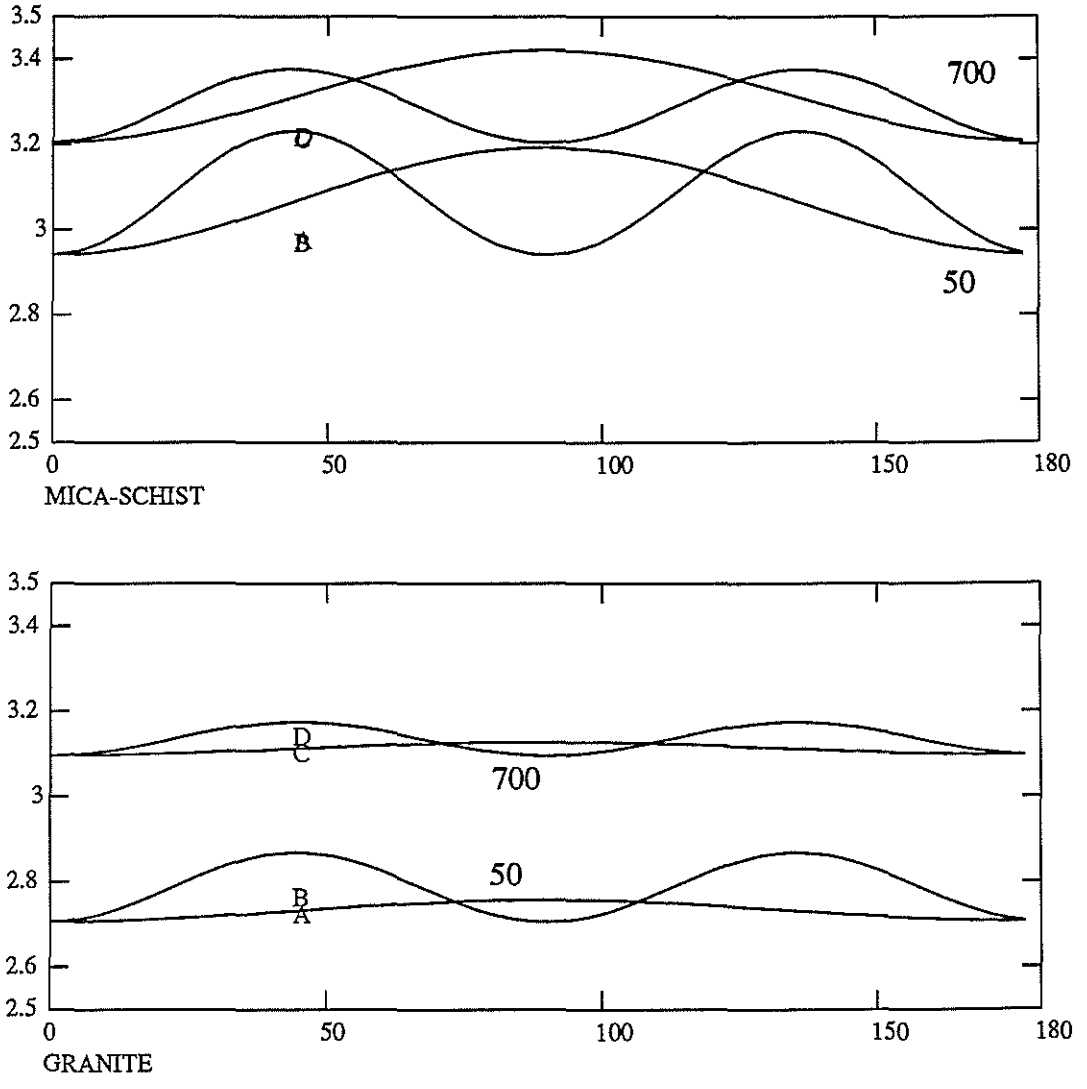

Figure 8: Transversely isotropic angular velocity dependence of S-waves, both samples, P_{eff}=50, 700 bars. Velocities in km/s. X-axis is angle above horizontal plane.

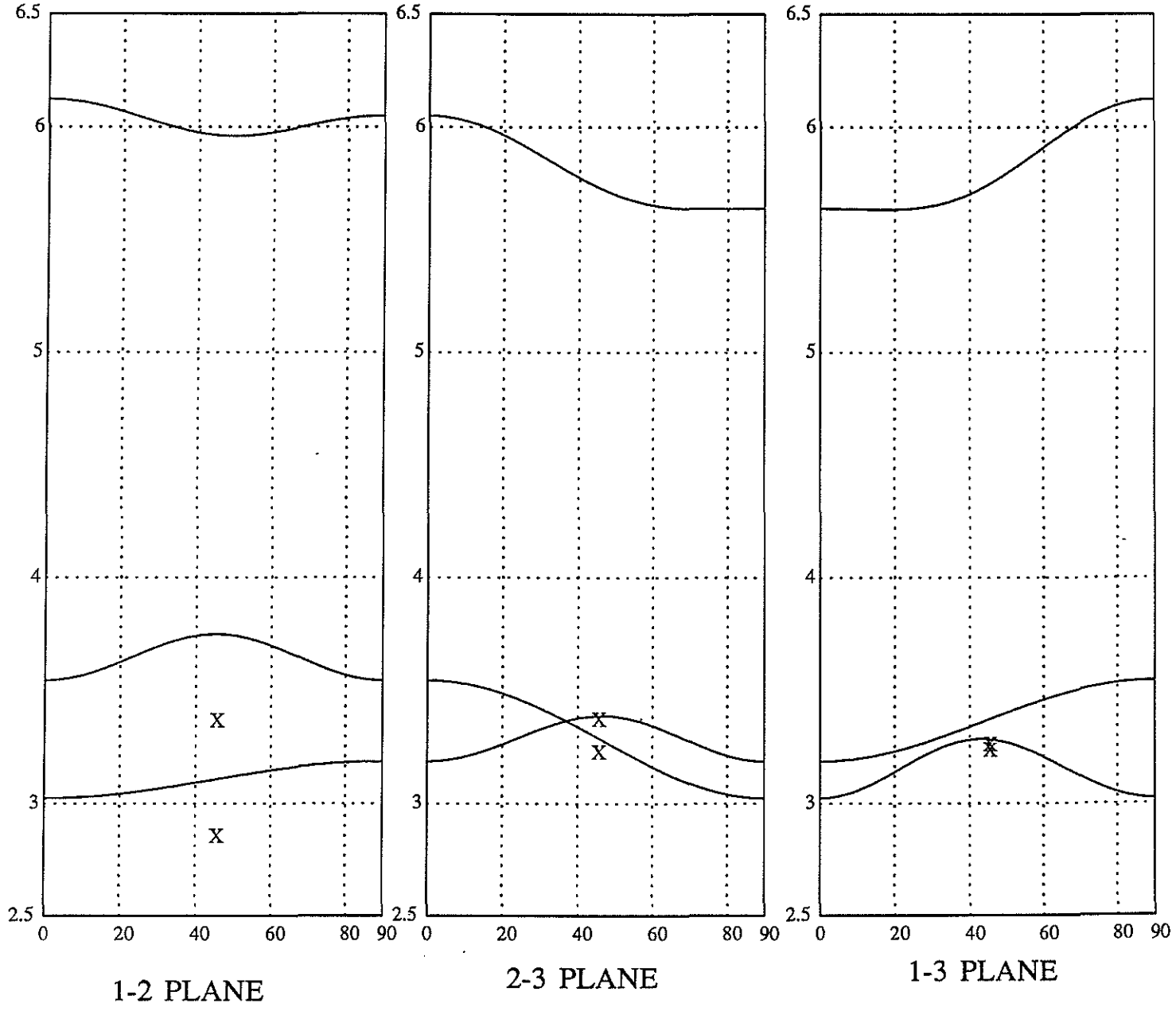

Figure 9: Orthorhombic angular velocity dependence for mica-schist sample at 700 bars P_{eff}. Velocities in km/s. Angles are in the principal planes, indicated.

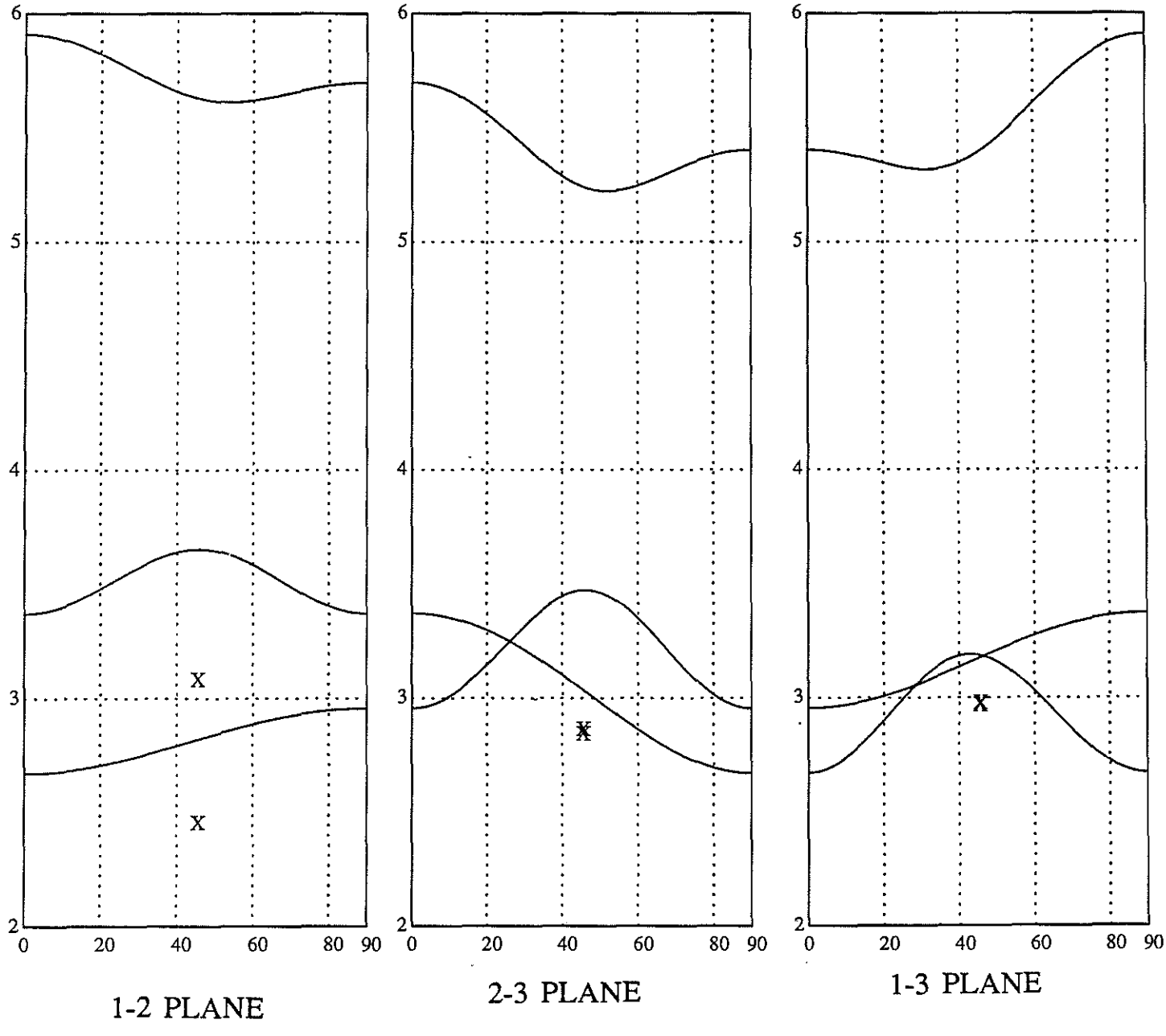

Figure 10: Orthorhombic angular velocity dependence for mica-schist sample at 50 bars P_{eff}. Velocities in km/s. Angles are in the principal planes, indicated.